Segmentation of Renal Perfusion Signals From Laser Speckle Imaging Into Clusters With Phase Synchronized Dynamics

Christopher G. Scully*, *Member, IEEE*, Nicholas Mitrou, Branko Braam, William A. Cupples, and Ki H. Chon, *Senior Member, IEEE*

***Abstract*—Renal perfusion signals contain dynamics arising from the renal autoregulation feedback mechanisms as the contraction and dilation of vessels alter flow patterns. We can capture the time-varying dynamics at points across the renal surface using laser speckle imaging. We segment an imaged area of the renal cortex into clusters with phase synchronized dynamics. Our approach first uses phase coherence with a surrogate data derived threshold to identify synchronized pixel pairs. Non-negative matrix factorization is then applied to segment phase coherence estimates into phase synchronized regions. The method is applied to laser speckle imaging of the renal cortex of anaesthetized rats to identify regions on the renal surface with phase synchronized myogenic activity. In three out of six animals imaged after bolus infusion of N^{ω}-nitro-l-arginine methyl ester (NAM), the renal surfaces are segmented into clusters with high phase coherence. No more than two clusters were identified during control period for any animal. In the remaining three animals, a strong myogenic signal could not be detected in surface perfusion during control or NAM. This method can be used to identify synchronization in renal autoregulation dynamics across the renal surface.**

***Index Terms*—Clustering, laser speckle imaging, renal autoregulation, synchronization.**

I. Introduction

RENAL blood flow is regulated by at least two feedback systems that operate within a nephron, the functional unit of the kidney. Afferent arterioles protect the glomerular capillaries and maintain glomerular filtration rate during blood pressure fluctuations by constricting and dilating in a process known as renal autoregulation. The two feedback mechanisms, the myogenic response (MR) and tubuloglomerular feedback (TGF), generate self-sustained oscillations in normotensive rats within ranges of 0.1–0.3 Hz and 0.02–0.05 Hz, respectively [1]. A human kidney contains ∼1 000 000 nephrons (∼30 000 in a rat). Although each nephron can be thought of as an independent unit, they are connected by a vascular tree stemming from the renal artery which branches into increasingly smaller vascular segments till reaching the afferent arteriole preceding each nephron [2]. Synchronization in TGF dynamics has previously been reported between neighboring nephrons in tubule pressure signals [3], [4] and renal perfusion signals obtained by laser speckle perfusion imaging (LSPI) [5]. The vascular tree that connects nephrons provides a cable for the transfer of information [6], and modeling studies have shown that vascular conduction can synchronize dynamics between nephrons [7], [8]. Such synchronization may contribute to renal autoregulation by the development of vascular resistance and spatial and temporal smoothing of blood flow and explain how autoregulation is able to adjust for blood pressure over a range larger than explained by the autoregulatory capacity of an individual nephron [9], [10]. There is therefore interest in being able to identify kidney vascular territories that have synchronized autoregulatory dynamics.

Evidence examining synchronization on a wide scale requires imaging approaches to monitor flow with sufficient spatial and temporal resolutions. LSPI provides information about temporal perfusion changes in the superficial vasculature across an imaged region [11]. We investigated LSPI for measuring renal perfusion across the cortex and found time-series could be extracted that contain the relevant autoregulation dynamics [12]. The operating frequencies of the MR and TGF can be tracked at each location as they vary over time, and the time-varying dynamics between any two locations can be analyzed by measures of phase coherence (PC) to detect synchronization [13]. It is then necessary to develop a framework that allows identification of regions with synchronized renal autoregulation to allow further investigations on the importance of synchronization in effective renal autoregulation.

We present a method for segmenting laser speckle image sequences of the renal cortex into regions with phase synchronized dynamics. Our two-step procedure first estimates PC from the time-varying autoregulation phases extracted from each pair of pixels, and these estimates are then clustered to identify synchronized regions. The method is illustrated with LSPI sequences of the renal cortex from anaesthetized rats.

Manuscript received October 11, 2013; accepted March 3, 2014. Date of publication March 11, 2014; date of current version June 14, 2014. This work was supported by Canadian Institutes of Health Research under Grant MOP-102694. The work of C. G. Scully was supported by an American Heart Association predoctoral fellowship. *Asterisk indicates corresponding author.*

*C. G. Scully was with the Department of Biomedical Engineering, Worcester Polytechnic Institute, Worcester, MA 01609 USA. He is now with the Office of Science and Engineering Laboratories, Center for Devices and Radiological Health, US Food and Drug Administration, Silver Spring, MD 20993 USA (e-mail: christopher.scully@fda.hhs.gov).

N. Mitrou and W. A. Cupples are with the Department of Biomedical Physiology and Kinesiology, Simon Fraser University, Burnaby, BC V5A 1S6, Canada (e-mail: nmitrou@sfu.ca; wcupples@sfu.ca).

B. Braam is with the Departments of Medicine and Physiology, University of Alberta, Edmonton, AB T6G 2R3, Canada (e-mail: branko.braam@ualberta.ca).

K. H. Chon is with the Department of Biomedical Engineering, Worcester Polytechnic Institute, Worcester, MA 01609 USA (e-mail: kichon@wpi.edu).

Color versions of one or more of the figures in this paper are available online at http://ieeexplore.ieee.org.

Digital Object Identifier 10.1109/TBME.2014.2311118

II. Materials and Methods

A. Experimental Methods

Experiments were performed in accordance with the guidelines of the Canadian Council on Animal Care and approved by the Animal Care Committee of Simon Fraser University. Long-Evans rats ($N = 7$) (Harlan, Livermore, CA, USA) were given buprenorphine (0.02 mg/kg i.p.) 20 min prior to being placed under anaesthesia with 4% isoflurane in inspired gas, then reduced to 2%. Each animal was placed on a heated table (35 °C) and the trachea cannulated for ventilation by a small animal respirator (TOPO, Kent Scientific, Torrington, CT, USA). The left kidney was exposed, freed from surrounding fat, and secured in a kidney cup anchored to the table. Grease was placed in the cup around the kidney to minimize motion.

LSPI was performed 1 h after kidney preparation using the moorFLPI laser speckle contrast imager (Moor Instruments, Axminster, UK). The moorFLPI illuminates the target surface with a 785 nm laser providing flow information for the most superficial nephrons in the renal cortex, ∼100 μm deep [14]. The resulting speckle pattern is captured with a charge-coupled device camera at a frame rate of 25 Hz. Flow changes in the tissue alter the speckle pattern such that higher flow blurs the pattern reducing the contrast and lower flow increases the contrast [15]. Contrast statistics of the pattern were computed over a spatial set of pixels resulting in a relative perfusion index mapped across the surface at 113 × 152 pixels and 25 Hz [15]. The lens was positioned ∼20 cm away from the kidney resulting in an imaging window of ∼5 × 7 mm. A ∼4 mm hair was placed on the renal surface to determine the pixel length, and the renal surface was monitored for ∼300 s for each animal. In $N = 6$ rats, imaging occurred before (CTL) and after bolus infusion of the nitric-oxide synthase inhibitor N^{ω}-nitro-l-arginine methyl ester (NAM) (Sigma-Aldrich, Oakville, ON, Canada) at 10 mg/$kg_{\mathrm{BODY\text{-}WEIGHT}}$.

After acquisition, flux image series were loaded into MATLAB r2011b (The Mathworks, Natick, MA) for processing. A Gaussian spatial filter (width of 8 pixels corresponding to –10 dB cutoff) was applied to each frame to increase the signal–noise ratio of the time-series at each pixel [16], and the filtered images were then spatially downsampled by a factor of 4 to reduce redundant information at adjacent pixels caused by the spatial filter. The size of the spatial filter was determined from a previous study where it was found to adequately identify autoregulation signals [12]. Time-series extracted from each pixel were low-pass filtered (0.5 Hz cutoff frequency) and downsampled to 1 Hz because the pertinent autoregulation frequencies are in the 0.01–0.3 Hz frequency range [1].

The peak power of the MR dynamic relative to background noise was computed using the detection ratio [see (1)]. In (1), P_{sig} is the peak power of the dynamic within the MR frequency range, 0.1–0.3 Hz, from the power spectrum. P_{noise} is mean power of the noise region, 0.3–0.5 Hz:

$$DR = 10\log_{10}\left(\frac{P_{\mathrm{sig}} - \bar{P}_{\mathrm{noise}}}{SD(P_{\mathrm{noise}})}\right). \tag{1}$$

B. Estimation of PC

The time-series extracted from each pixel within the LSPI videos are analyzed for the changes in the temporal relationships in renal autoregulation dynamics between pixels. The first step is to estimate PC for the MR or TGF dynamic between every pixel pair. To the extent that perfusion dynamics from two locations are synchronized, the phase difference between the two should remain constant over time. PC is bounded by 0 (no phase relationship) and 1 (signals are phase locked), but what constitutes significant PC between these extremes can be open ended. A significance threshold derived from surrogate data is used to determine if the observed PC is statistically different from the PC values of two signals with similar time-varying dynamics but with phase relationships destroyed.

To determine PC between two signals, the instantaneous phases for each are estimated. Each signal is bandpass filtered for the MR range using a forwards–backwards Butterworth filter to preserve phase relationships in the signals. For the MR frequency range, a 16th-order filter with low- and high-cutoff frequencies of 0.09 and 0.32 Hz, respectively, is used to isolate the dynamic. After bandpass filtering, the Hilbert transform is applied to find the analytic signal and subsequently determine the instantaneous frequency at all time points, $f(t)$. Ideally, the instantaneous frequency will remain between the cutoff frequencies of the bandpass filters, but phase slips can occur that cause the frequency to jump outside of the range of the bandpass filter [13]. These phase slips are induced by noise present in the signal that is unrelated to the autoregulation frequencies, interrupting the continuous autoregulation signal. Locations where the instantaneous frequency has extended beyond the bandpass filter cutoff frequencies are identified and linearly interpolated to ensure that all instantaneous frequencies are within the passband of the filters [13]. The instantaneous phase, $\varphi(t)$, is the integral of the instantaneous frequency and wrapped between $-\pi$ and π. PC is then computed between two signals, m and j, as the mean over N data points of their exponential difference in phase [17]:

$$PC_{mj} = \left|\frac{1}{N}\sum_{l=1}^{n} e^{i(\varphi_{jl} - \varphi_{ml})}\right|. \tag{2}$$

To determine the significance of PC between the extremes, we apply a surrogate data-derived threshold to test the null hypothesis that the instantaneous phase relationships between the signals are independent of time [13]. The surrogate data-derived threshold provides an expected PC for the two signals that is dependent on the dynamics of the signals but independent of the timing of the recorded signals. The instantaneous frequency of one of the two signals is circularly shifted a random distance in time (n) to destroy phase relationships between the two signals as

$$f_{\mathrm{surr}}(t) = \begin{cases} f(t-n) & n+1 \le t \le N \\ f(N-n+t) & 1 \le t \le n. \end{cases} \tag{3}$$

$f_{\mathrm{surr}}(t)$ is used to estimate the surrogate instantaneous phases, $\varphi_{\mathrm{surr}}(t)$. This procedure removes phase relationships between the two signals but maintains the signal dynamics [13]. PC is

then estimated between $\varphi_{\mathrm{surr}}(t)$ and $\varphi(t)$ from the signal the surrogate procedure is not performed on. Fifty surrogate PC estimates are made, and the significance threshold is set as the mean plus 2 standard deviations of the surrogate PC estimates. Two signals are declared as having significant PC if greater than this threshold.

C. Identification of Synchronized Clusters

PC and significance levels are determined between every pair of pixels and combined into a single $n \times n$ synchronization matrix, where n represents the total number of pixels. The synchronization matrix, R, contains bivariate synchronization indices, PC, between all pairs of pixels [18]. R_{mj} is the PC between pixel m and j. If pixels m and j did not have significant PC determined by the surrogate threshold, R_{mj} is set to 0.

The mean PC of R is reported for each animal. A high mean PC indicates homogenous synchronization across the surface. The interpretation of a low mean PC may be: 1) phase synchronization of the dynamics of interest is not present across the surface; and 2) phase synchronization is present in local areas only but low at locations further away. The coefficient of variation (CV, standard deviation of PC divided by mean PC) of R is reported as a measure of the homogeneity of PC across the kidney surface.

Non-negative matrix factorization (NMF) was used to reduce the $n \times n$ synchronization matrix R into two matrices W $(n \times r)$ and H $(r \times n)$ using an iterative computation subject to the constraint that all values in W and H are ≥ 0 [19]. Because W and H are positive, only additive combinations are possible which allows sparse components to be generated. R is the $n \times n$ symmetric synchronization matrix containing PC values between 0 and 1. r represents the rank of the reduced matrices to be determined. By varying the rank r, the number of clusters to be identified can be adjusted

$$R \approx WH. \tag{4}$$

NMF was performed with update equations based on the squared error between R and WH [20]

$$Err = \|R - WH\|^2. \tag{5}$$

One hundred initial starting points were used and r was varied from 1 to 10. The difference in (5) for increasing the rank by 1 was used as the criterion for determining the cluster number [21]. When the result of increasing r by 1 was a change in the residual error ($|Err_{r+1} - Err_r|$) of less than 0.01, the number of clusters was set to r.

To assign clusters, W is generally used to represent bases that can be used to reconstruct R from the encoding in H [22]. Because the synchronization matrix is symmetric, the cluster that makes up the largest contribution of the data at each pixel is used to determine the cluster assignments, (6), where j represents the pixel and r the cluster. In this way, each pixel is assigned to the cluster that makes up the largest additive portion of the original PC. If W and H are sparse and there is separation between clusters, the additive component from the strongest cluster will have a significant contribution

$$\mathrm{Cluster}(j) = \arg\max_r (W_{jr} H_{rj}). \tag{6}$$

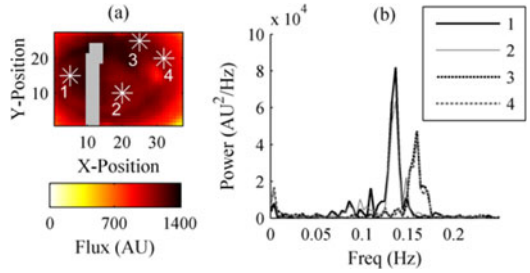

Fig. 1. (a) Time-averaged laser speckle perfusion image of the renal cortex. The gray bar represents the 4 mm hair placed across the renal cortex. (b) Frequency spectra of the extracted time-series from the four locations denoted by a star in (a).

III. Results

A. Example Identification of Clusters

Fig. 1(a) shows the time-averaged flux at each downsampled pixel for the single animal that did not receive NAM, and Fig. 1(b) shows the flux spectra from the four white star locations in Fig. 1(a). Locations were selected to demonstrate the approach with two locations each sharing the same frequency. Frequencies between 0.1 and 0.2 Hz in Fig. 1(b) can be identified as the MR signature. Two signals have a dominant frequency around 0.13 Hz and the other two signals have a dominant frequency >0.15 Hz. It might be expected that signals sharing the same frequency are synchronized, but this is not guaranteed since renal autoregulation dynamics are highly time varying and instantaneous phase changes may be uncorrelated between the two signals [23], [24]. For this reason, we estimate the PC by evaluating the temporal variations in the phase difference between the two signals using PC and compare to a significance test.

PC and significance level estimates are determined between the time-series from all pixel pairs and maps of PC between each pixel and all others are generated. Fig. 2(a)–(d) shows PC maps for the four example locations marked in Fig. 1. In each frame of Fig. 2, PC between the time-series from every pixel and the pixel identified with the white star is displayed. Combinations of pixels without significant PC are set to 0.

Fig. 2(a) shows that signal 1 has significant PC with all other pixels within the large shaded region. From Fig. 2(b), we see that signal 2 has significant PC with the same pixels as signal 1 and this large shaded area corresponds to a synchronized cluster. In Fig. 2(c) and (d), we see that signals 3 and 4 have significant PC with each other within a second cluster. Visualizing these surface maps is useful to gain an understanding of the PC distribution across the surface, and clustering analysis can be applied to find groups of synchronized pixels [25].

PC values between all pairs of pixels from our LSPI data of the renal cortex were transformed into a single synchronization matrix and the clustering method applied. Fig. 3(a) shows the frequency with the maximum spectral power in the MR

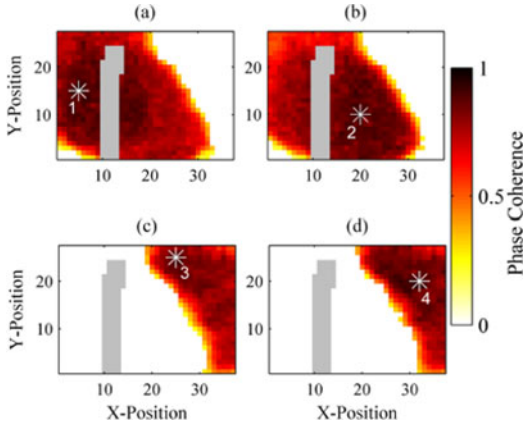

Fig. 2. (a) PC between signal 1, marked by the white star, and all other pixels. The gray bar represents the wire placed on the surface, and white space indicates nonsignificant PC as determined by the surrogate significance threshold. (b)–(d) PC estimates relative to the pixel marked by the white star in each frame. The stars and numbers correspond with the locations in Fig. 1.

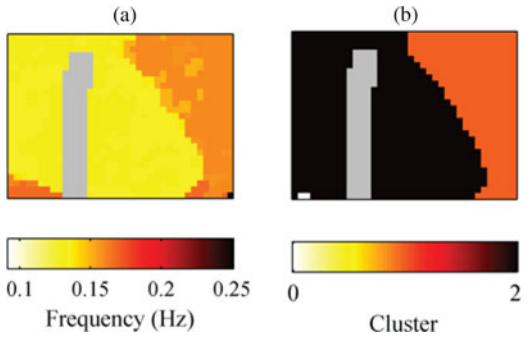

Fig. 3. (a) Frequency with the maximum power within the MR range (0.09–0.3 Hz) at each pixel location. (b) Cluster maps identified by NMF of the synchronization matrix. Pixels with the same color are assigned to the same cluster. Data are for the same animal as in Figs. 1 and 2.

frequency range for the time-series extracted from each pixel. Fig. 3(b) displays the cluster map using NMF. Clusters < 9 adjacent pixels in size are ignored, as this size can correspond to the Gaussian spatial filter. The method clusters the PC values seen in Fig. 2 similar to the frequency mapping in Fig. 3(a). The two large clusters are $\sim$8.1 and 17.2 mm^2.

B. *Effect of Signal Characteristics on PC*

Meaningful estimates of PC and the significance level depend on appropriate signal length and strength of the dynamic relative to background noise. To demonstrate the influence of these characteristics, we selected 100 pairs of signals within the large synchronized region in Fig. 2(a) and (b), and another 100 pairs where one of the signals belongs to the synchronized region in Fig. 2(a) and (b) and the other belongs to the region in Fig. 2(c) and (d). The signals were selected from locations evenly dispersed across each region.

PC and significance levels were determined between each pair for data lengths increasing from the first 50 s of the signals up until the full data length (340 s). Mean and 95% confidence intervals over the pairs of synchronized and nonsynchronized signals were determined for the PC and significance levels,

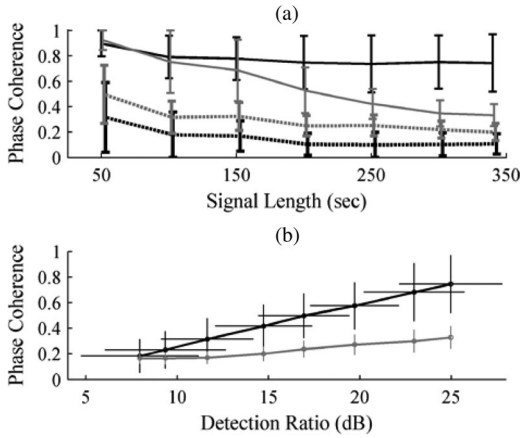

Fig. 4. (a) Impact of data length on PC and significant thresholds. Solid lines are mean and 95% confidence intervals for 100 pairs of signals belonging to the same coupled region. Dashed lines are the same for 100 pairs of signals belonging to different regions (nonphase coupled signals). Black lines represent the PC and gray lines significance thresholds. (b) Impact of white noise on PC. Solid black line is PC computed between pairs of pixels expected to belong to the same cluster for varying levels of noise added with 95% confidence intervals on PC (vertical error bars) and detection ratio (horizontal error bars). The gray line represents significance thresholds with 95% confidence levels over the 100 pairs.

Fig. 4(a). PC and significance thresholds are higher at short data lengths, and there is poor separation between the true PC and surrogate-derived significance thresholds at this point. As the data length increases to $>$250 s, there is clear identification of the synchronized pairs. For nonsynchronized pairs, dashed lines in Fig. 4(a), the separation between significance levels and PC is relatively constant at data lengths greater than 150 s.

White noise was added in increasing amplitudes [0, 0.5, 1, 1.5, 2, 3, 4, 5] to the signals after normalization by the signal variance. PC and significance levels were estimated at each noise level as was the detection ratio for each signal plus noise combination. The detection ratio was averaged between the two signals in each pair. Mean and 95% confidence intervals are shown in Fig. 4(b) of PC and significance levels as functions of the detection ratio for increasing noise levels for the pairs with significant PC. Horizontal error bars represent 95% confidence intervals of the detection ratio for the 100 signal pairs. With no noise added, the MR dynamic has a detection ratio of $\sim$25 dB between all pairs of signals. As the detection ratio decreases due to added noise, PC and significance levels decrease. At detection ratios $<$10 dB, there is poor separation between PC and significance levels, and accurate estimates of significant PC cannot be made. Results are not shown for the nonsynchronized signal pairs as PC and significance levels had insignificant changes for increasing levels of added noise. As the signal characteristics change from data length and noise, PC values vary. Surrogate data adapts the significance threshold to varying signal characteristics.

C. *Identified Clusters*

The frequency spectrum for the mean laser speckle signal (average of time-series across all pixels) for the six animals before and after NAM is presented in Fig. 5(a) and (b), respectively.

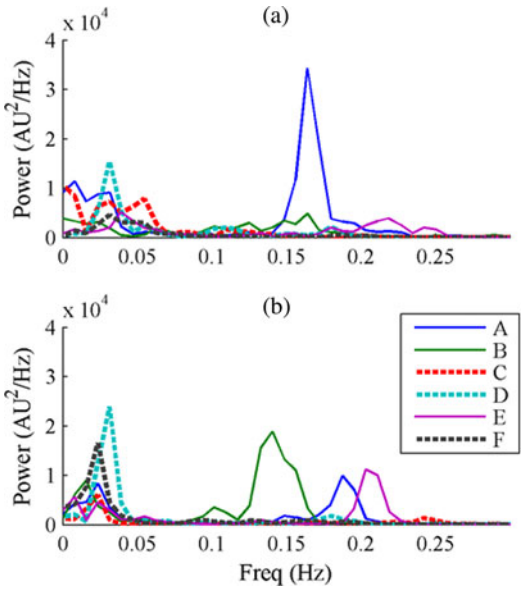

Fig. 5. Power spectra of the laser speckle time-series averaged over all pixels for six animals during (a) CTL and (b) NAM. Solid lines indicate animals with maximum frequency power in the range of the MR, and thick dashed lines indicate animals with maximum frequency power in the range of TGF.

TABLE I
STATISTICS OF SYNCHRONIZATION MATRIX

		A	B	C	D	E	F
CTL	Mean	0.5	0.64	0.35	0.36	0.34	0.27
	CV	0.13	0.16	0.33	0.22	0.21	0.3
NAM	Mean	0.45	0.33	0.41	0.33	0.43	0.41
	CV	0.45	0.53	0.21	0.29	0.50	0.18

CV = coefficient of variation.

Three animals, A, B, and E, have dominant spectral power in the MR range from 0.1 to 0.25 Hz during CTL and NAM, Fig. 5(b). The remaining three animals, C, D, F, are dominated by lower frequency content $<$0.05 Hz, representative of TGF during CTL and NAM.

The mean PC and CV of the synchronization matrix for each animal during CTL and NAM periods is reported in Table I.

Fig. 6 shows the dynamic characteristics during CTL and NAM mapped for the three animals with strong MR signal. Each row contains the dominant frequency in the MR range mapped at each pixel, detection ratio of that frequency, cluster map, and PC for each pixel with the pixel at the geometric centroid of the cluster it belongs to for one animal either during CTL or NAM as labeled.

Fig. 7(a) and (b) shows PC maps for the two locations labeled by the white star in Fig. 6, row B (Animal A during NAM). The two locations do not have significant PC with each other although they do share the same dominant frequency as seen in the first column of Fig. 6, row B. The locations they do have significant PC with correspond to the cluster map in Fig. 6, row B. It has previously been shown that the renal autoregulation dynamics are highly time varying [23], and the time variance for the two signals can be visualized in the time–frequency representations, generated by Variable Frequency Complex Demodulation [26], in Fig. 7(c) and (d). Even though the locations share a dominant frequency, the time variance of each differs and therefore PC, which tracks how consistent the phase relationships are over time, is not significant.

Characteristics of the clusters were quantified and compared to the detection ratios of the dynamics in Fig. 8. PC averaged between all pairs of pixels within each cluster ($\mathrm{PC_{MEAN}}$) is shown on the y-axis in Fig. 8(a) with the x-axis representing the detection ratio averaged across all pixels within that cluster. The approximate physical areas ($\mathrm{mm^2}$) corresponding to each cluster are presented in Fig. 8(b) against the detection ratio. Animals A, B, and E form the most clusters (3, 6, and 4, respectively) during NAM with high detection ratios and $\mathrm{PC_{MEAN}}$ within those clusters. More clusters are identified in B than A or E, but the field of view is larger for B and clusters are similar in physical size. No animal forms more than two clusters during CTL.

D. Limitation to Size of Cluster Identification

The smallest clusters that can be identified are a function of the physical area captured by the pixels and the spatial averaging filter applied to increase signal strength for accurate PC estimates. For each imaging file, two groups of 10 pixels from the same cluster and another group of 10 pixels from a separate cluster were selected. The two groups of pixels from within the same cluster were considered synchronized and the groups from separate clusters were considered unsynchronized. The selected pixels within each cluster were approximately equidistant apart. An $N \times N$ averaging window was applied to each frame centered on the selected pixels from the original 113 $\times$ 152 moorFLPI flux data to generate time-series for a range of window sizes ($N = 2{:}9$). For each N, the detection ratio of the MR in the time-series was determined for each pixel as was PC between the pairs of synchronized and unsynchronized pixels. The accuracy of identifying pixel pairs as either synchronized or unsynchronized using the surrogate data threshold was found at each N as the number of pairs from the same cluster identified as synchronized plus the number of pixel pairs from separate clusters identified as unsynchronized, divided by the total number of pairs. This procedure was performed on the NAM data where an average detection ratio of the MR signal was $>$15 dB using the Gaussian spatial filter. The remaining data files did not have a detectable MR signal. This provided four datasets: the control example describing the procedure in Section II-A and records A, B, and E from the NAM group in Section II-C.

The amplitude of the MR signal increases when larger pixel areas are averaged together, Fig. 9(a). PC between synchronized pixel pairs (those identified within the same cluster using the Gaussian spatial filter) increases as larger areas are averaged, but PC between unsynchronized pixel pairs does not, Fig. 9(b). Fig. 9(c) shows the relationship between the detection ratio and PC as the size of the averaging window is adjusted. Fig. 9(d) shows the accuracy of identifying pixel pairs as synchronized or unsynchronized as a function of the averaging width.

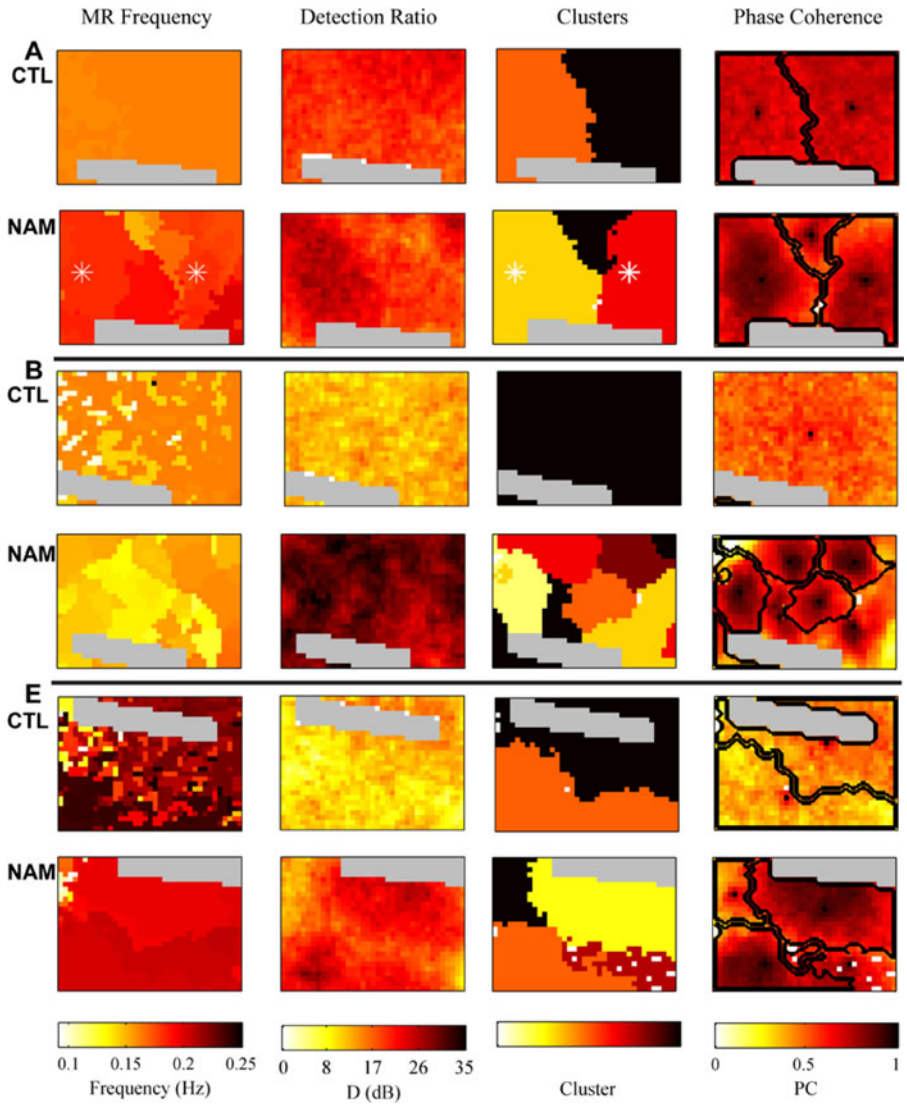

Fig. 6. Characteristics of the MR signal and PC-based clustering during CTL and NAM for the three animals showing MR signal (A, B, and E). Each row represents one imaging period. The first column shows the peak MR frequency, second column the detection ratio for that frequency relevant to background noise, third column the maps of clusters determined using NMF, and the fourth column maps of the PC relative to the signal at the geometric centroid of each cluster.

IV. Discussion

We have presented an approach for identifying phase synchronized regions in LSPI of the renal cortex by clustering PC estimates between all pairs of pixels. The applied clustering algorithms utilize only the PC coefficients without any spatial information and identified clusters consisted of adjacent pixels. When applying the method to renal autoregulation data, clusters with phase synchronized MR dynamics were identified.

Efferent arterioles leave the glomerulus and approach the renal surface where they diverge into a series of vessels producing a "star" structure [2]. Flow in efferent "star" vessels contain renal autoregulation dynamics [27]. Due to the penetration depth of the lasers in this study, placement of "star" vessels in the subcapsule region, and higher red blood cell velocity in arterioles than capillaries, efferent arterioles are likely the predominant contributors to speckle signals of renal cortical blood flow [5]. In this way, two nephrons connected by preglomerular vasculature at a distance up to 600 μm may have efferent star vessels that take up a significantly larger space on the renal surface that is captured with LSPI. TGF synchronization between pairs of nephrons connected in the preglomerular vasculature across distances up to 600 μm has previously been reported [3]. Additional nephrons may synchronize their activity to form clusters [9].

The presented approach relies on the analysis of spontaneous oscillations in blood flow generated by the renal autoregulation feedback mechanisms, namely the MR as presented here. Such spontaneous oscillations have been repeatedly reported in the literature [1], [28], [29]. However, in the present set of six animals, the presence of the MR signal varied considerably. From Fig. 8(a), it is seen that a higher detection ratio corresponds to higher $\mathrm{PC}_{\mathrm{MEAN}}$. In three animals, a strong MR was identified during NAM with one of those three also showing a strong signal during CTL. In the remaining three animals, the MR signal had a low detection ratio during CTL and NAM, but frequency

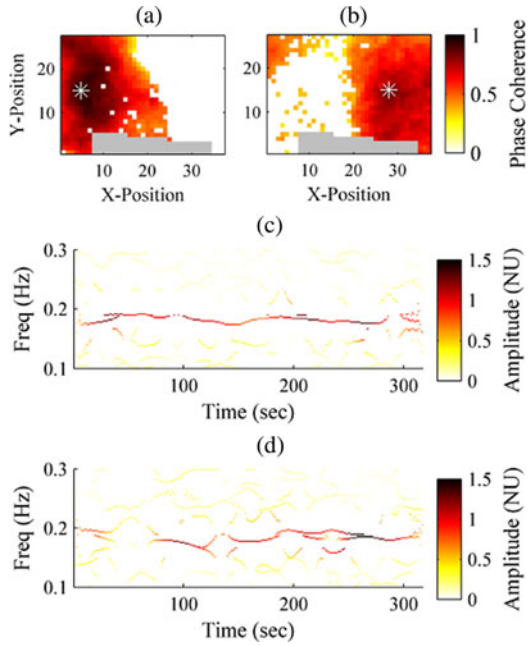

Fig. 7. (a) PC between time-series from pixel marked by the white star and all other pixels from Fig. 6, second row. White space indicates locations that do not have significant PC with the white star. (b) PC between pixel with second white star and all other pixels. (c) and (d) Time–frequency spectra in the MR frequency range for the time-series from the white stars in (a) and (b).

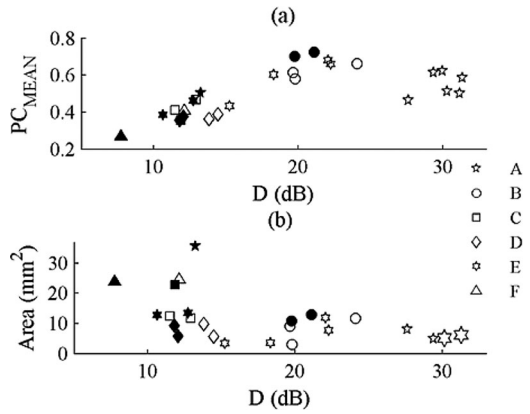

Fig. 8. Characteristics of identified clusters for the six animals during CTL (open) and NAM (filled). Each animal is designated by a different symbol and the results are plotted for each cluster from that animal. (a) Average PC within each cluster versus the detection ratio averaged over all time-series from the pixels within that cluster. (b) Measured physical area of each cluster versus the average detection ratio. The enlarged markers (b) represent two overlapping data points.

content in the expected TGF range was visible in the spectra, Fig. 5. These animals were all of the same strain and received the same bolus infusion of NAM; however, their renal autoregulation dynamics showed considerable differences. This lack of a signal is representative only of the imaged region of the vasculature and does not mean that the MR was lacking in the animal.

Without a dominant MR signal, we cannot expect to identify significant PC between locations. This is reinforced by looking at the CV of PC values in the synchronization matrix. Although all animals had relatively low mean PC across the synchronization matrix ranging from 0.33 to 0.45 during NAM, the three animals with a dominant MR signal each had a CV of the synchronization greater than any of the three animals lacking a dominant MR signal during NAM. This indicates a difference in the distribution of PC values across the renal surface. For the three animals lacking the MR signal, less variability indicates a more homogenous surface of low PC, while the three animals with the MR signal a higher CV indicates that there is considerable variability across the surface with local areas with high PC. A and B both showed higher PC across the surface during CTL than NAM, but CV was less and resulting in a lower number of clusters being identified. It is this pattern of PC across the surface that is further described through clustering analysis.

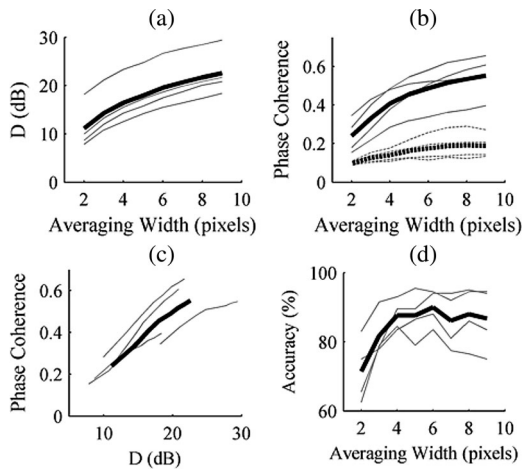

Fig. 9. (a) Detection ratio averaged over all selected pixels as a function of the $N \times N$ window size. Thin lines represents individual NAM files with detection ratios >15 dB, the thick black lines represent the mean of the four files. (b) PC between pixel pairs with significant PC (solid lines) and without significant PC (dashed lines) as a function of the $N \times N$ window size. (c) PC as a function of the detection ratio. (d) Accuracy of correctly identifying pixel pairs with significant PC using the surrogate data thresholds.

The surface was segmented into more than two clusters for the three animals showing an MR signal after NAM. The cluster locations were not necessarily in agreement with the frequency map generated by identifying the maximum frequency at each location, showing the alternative information gained by considering the time-varying dynamics. Fig. 8(a) shows how the PC within each cluster is higher for these animals than for the animals without an MR signal, and is also higher than the mean PC for each animal. This indicates strong, localized synchronization of the MR.

NAM has previously been shown to alter the MR response [30], [31]. It is known that NAM affects vascular smooth muscle cells a number of ways including sensitization of Ca^{2+} [32], activation of voltage dependent K^{+} channels [33] and potentially influencing vascular communication through gap junctions [34]. For these reasons, we infused NAM with the expectation it would alter the observed clusters. Although there tended to be an increase in the number of clusters during NAM when an MR signal was present, because only three animals showed a strong MR signal, additional studies are needed to confirm that there is an effect of NAM.

Holstein-Rathlou *et al*. tracked the TGF dynamics in the superficial vasculature across the renal cortex with LSPI [5]. They clustered the time-varying dynamics across the surface using hierarchical clustering [5] to find signal pairs with similar time variance. In this study, we identified synchronized MR regions and generated images of the segmentation of perfusion dynamics across the surface. The phase synchronized MR regions identified were on the scale of 5–10 mm^2 during NAM which may indicate the synchronization of greater than ten lobules. To accomplish this, communication may occur through electrotonic responses that have shown to be present in renal vasculature or hemodynamic coupling [6]. At this time, the exact mechanism of synchronization requires further study. Synchronization of the MR dynamic has not been extensively studied, although the MR is both necessary and sufficient for effective autoregulation [1], [9].

A. Limitations

The detectable cluster size is restricted by our effective pixel resolution and field of view allowed by the moorFLPI imaging system. In this study, our field of view was set at $\sim$5 mm $\times$ 7 mm corresponding to approximately one-third of the posterior surface of the kidney. By reducing the zoom, we could capture the entire surface, but in doing so would increase the size of our effective spatial resolution. As presented, this resolution is set to capture flow in efferent star vessels related to individual nephron dynamics that are considered to be the independent unit contributing to clusters. Although the physical distance captured by a flux pixel in our imaging setup is $\sim$40 μm, individual pixels do not provide MR signals with significant amplitude so an averaging window must be applied. Low detection ratios lead to low PC estimates, Fig. 4(b), resulting in poor accuracy of cluster identification, Fig. 9. From Fig. 9, the smallest spatial filter that provides a detection ratio $>$15 dB should be used and this corresponded to a 4 $\times$ 4 pixel window that represents a $\sim$160 $\times$ 160 μm^2 region on the renal surface.

When low detection ratios were present in real data, Fig. 6 C, D, and F, the surfaces were segmented into one or two clusters with low PC amongst the pixels in each cluster. These clusters should not be interpreted as being synchronized, as the PC is low and without a strong signal the PC is more representative of noise than MR. Signal quality should be considered when interpreting clusters.

We found it necessary to have at least 20 oscillations to determine significant PC using the surrogate data approach. This translates to $\sim$3–5 min of data for the MR or $\sim$20–25 min for TGF. For this reason, we only investigated the MR here. Given longer datasets, TGF synchronization can be estimated alongside the MR.

Three clustering methods were initially investigated to apply to the synchronization matrices. Simulation studies (not shown) using the eigendecomposition or spectral clustering approaches described in [18] and [25], respectively, showed equivalent results to the NMF method presented. NMF was reported because it allows for sparse combinations of pixels, but various clustering approaches can be applied. Computational complexity of NMF increases with the size of the synchronization matrix, which grows with the size of the input image used. In this study, we used the squared error update method, but alternative NMF algorithms are available that may reduce processing time [20]. These, or other clustering methods, may be more appropriate for larger images.

V. Conclusion

Renal surfaces can be segmented into regions with high coupling when strong dynamics are present by applying the described analytical approach to LSPI data. The approach identifies temporal synchronization between spatial locations by comparing time-varying changes in perfusion signals and then using clustering analysis to segment the surface. Dynamics present in surface perfusion signals are generated by the renal autoregulation mechanisms and synchronization across a large region of the renal surface may signify coordinated activity among a number of nephrons. The presented approach enables studies to determine factors influencing synchronization across the renal surface and to understand how coordinated renal autoregulation contributes to highly effective kidney blood flow regulation.

References

[1] W. A. Cupples and B. Braam, "Assessment of renal autoregulation," *Amer. J. Physiol. Renal Physiol.*, vol. 292, pp. F1105–F1123, Apr. 2007.
[2] R. Beeuwkes III, "Efferent vascular patterns and early vascular-tubular relations in the dog kidney," *Amer. J. Physiol.*, vol. 221, pp. 1361–1374, 1971.
[3] K. P. Yip, N. H. Holstein-Rathlou, and D. J. Marsh, "Dynamics of TGF-initiated nephron-nephron interactions in normotensive rats and SHR," *Amer. J. Physiol. Renal Physiol.*, vol. 262, pp. F980–F988, Jun. 1, 1992.
[4] N. H. Holstein-Rathlou, "Synchronization of proximal intratubular pressure oscillations: Evidence for interaction between nephrons," *Pflugers Arch.*, vol. 408, pp. 438–443, 1987.
[5] N. H. Holstein-Rathlou, O. V. Sosnovtseva, A. N. Pavlov, W. A. Cupples, C. M. Sorensen, and D. J. Marsh, "Nephron blood flow dynamics measured by laser speckle contrast imaging," *Amer. J. Physiol. Renal Physiol.*, vol. 300, pp. F319–F329, Feb. 1, 2011.
[6] D. J. Marsh, I. Toma, O. V. Sosnovtseva, J. Peti-Peterdi, and N.-H. Holstein-Rathlou, "Electrotonic vascular signal conduction and nephron synchronization," *Amer. J. Physiol. Renal Physiol.*, vol. 296, pp. F751–F761, Apr. 2009.
[7] D. D. Postnov, D. E. Postnov, D. J. Marsh, N. H. Holstein-Rathlou, and O. V. Sosnovtseva, "Dynamics of nephron-vascular network," *Bull. Math. Biol.*, vol. 74, pp. 2820–2841, 2012.
[8] D. J. Marsh, A. S. Wexler, A. Brazhe, D. E. Postnov, O. V. Sosnovtseva, and N.-H. Holstein-Rathlou, "Multinephron dynamics on the renal vascular network," *Amer. J. Physiol. Renal Physiol.*, vol. 304, pp. F88–F102, Jan. 2013.
[9] W. A. Cupples, "Interactions contributing to kidney blood flow autoregulation," *Curr. Opin. Nephrol. Hypertens.*, vol. 16, pp. 39–45, 2007.
[10] W. Cupples, A. S. Wexler, and D. J. Marsh, "Model of TGF-proximal tubule interactions in renal autoregulation," *Amer. J. Physiol.-Renal Physiol.*, vol. 259, pp. F715–F726, 1990.
[11] D. A. Boas and A. K. Dunn, "Laser speckle contrast imaging in biomedical optics," *J. Biomed. Opt.*, vol. 15, pp. 011109–011112, 2010.
[12] C. G. Scully, N. Mitrou, B. Braam, W. A. Cupples, and K. H. Chon, "Detecting physiological systems with laser speckle perfusion imaging of the renal cortex," *Amer. J. Physiol. Regul. Integr. Comparative Physiol.*, vol. 304, pp. R929–R939, Jun. 1, 2013.
[13] J. M. Hurtado, L. L. Rubchinsky, and K. A. Sigvardt, "Statistical method for detection of phase-locking episodes in neural oscillations," *J. Neurophysiol.*, vol. 91, pp. 1883–1898, 2004.
[14] R. Bezemer, M. Legrand, E. Klijn, M. Heger, I. C. Post, T. M. van Gulik, D. Payen, and C. Ince, "Real-time assessment of renal cortical

microvascular perfusion heterogeneities using near-infrared laser speckle imaging," *Opt. Exp.*, vol. 18, pp. 15054–15061, 2010.

[15] J. O'Doherty, P. McNamara, N. T. Clancy, J. G. Enfield, and M. J. Leahy, "Comparison of instruments for investigation of microcirculatory blood flow and red blood cell concentration," *J. Biomed. Opt.*, vol. 14, p. 034025, 2009.

[16] S. Bricq, G. Mahé, D. Rousseau, A. Humeau-Heurtier, F. Chapeau-Blondeau, J. Rojas Varela, and P. Abraham, "Assessing spatial resolution versus sensitivity from laser speckle contrast imaging: Application to frequency analysis," *Med. Biol. Eng. Comput.*, vol. 50, pp. 1017–1023, 2012.

[17] F. Mormann, K. Lehnertz, P. David, and C. E. Elger, "Mean phase coherence as a measure for phase synchronization and its application to the EEG of epilepsy patients," *Phys. D: Nonlinear Phenom.*, vol. 144, pp. 358–369, 2000.

[18] C. Allefeld, M. Müller, and J. Kurths, "Eigenvalue decomposition as a generalized synchronization cluster analysis," *Int. J. Bifucation Chaos*, vol. 17, pp. 3493–3497, 2007.

[19] D. D. Lee and H. S. Seung, "Learning the parts of objects by non-negative matrix factorization," *Nature*, vol. 401, pp. 788–791, 1999.

[20] M. W. Berry, M. Browne, A. N. Langville, V. P. Pauca, and R. J. Plemmons, "Algorithms and applications for approximate nonnegative matrix factorization," *Comput. Stat. Data Anal.*, vol. 52, pp. 155–173, 2007.

[21] K. Devarajan, "Nonnegative matrix factorization: An analytical and interpretive tool in computational biology," *PLoS Comput. Biol.*, vol. 4, p. e1000029, 2008.

[22] J. P. Brunet, P. Tamayo, T. R. Golub, and J. P. Mesirov, "Metagenes and molecular pattern discovery using matrix factorization," *Proc. Nat. Acad. Sci. USA*, vol. 101, pp. 4164–4169, 2004.

[23] K. H. Chon, Y. Zhong, L. C. Moore, N. H. Holstein-Rathlou, and W. A. Cupples, "Analysis of nonstationarity in renal autoregulation mechanisms using time-varying transfer and coherence functions," *Amer. J. Physiol. Regul. Integr. Comparative Physiol.*, vol. 295, pp. R821–R828, Sep. 2008.

[24] C. G. Scully, K. L. Siu, W. A. Cupples, B. Braam, and K. H. Chon, "Time–frequency approaches for the detection of interactions and temporal properties in renal autoregulation," *Ann. Biomed. Eng.*, vol. 41, pp. 172–184, Jan. 1, 2013.

[25] C. Allefeld and S. Bialonski, "Detecting synchronization clusters in multivariate time series via coarse-graining of Markov chains," *Phys. Rev. E*, vol. 76, p. 066207, 2007.

[26] H. Wang, K. L. Siu, K. Ju, and K. H. Chon, "A high resolution approach to estimating time–frequency spectra and their amplitudes," *Ann. Biomed. Eng.*, vol. 34, pp. 326–338, 2006.

[27] N. H. Holstein-Rathlou and P. P. Leyssac, "Oscillations in the proximal intratubular pressure: A mathematical model," *Amer. J. Physiol. Renal Physiol.*, vol. 252, pp. F560–F572, Mar. 1, 1987.

[28] K. P. Yip, N. H. Holstein-Rathlou, and D. J. Marsh, "Mechanisms of temporal variation in single-nephron blood flow in rats," *Amer. J. Physiol. Renal Physiol.*, vol. 264, pp. F427–F434, Mar. 1, 1993.

[29] W. A. Cupples, P. Novak, V. Novak, and F. C. Salevsky, "Spontaneous blood pressure fluctuations and renal blood flow dynamics," *Amer. J. Physiol. Renal Physiol.*, vol. 270, pp. F82–F89, Jan. 1, 1996.

[30] X. Wang and W. A. Cupples, "Interaction between nitric oxide and renal myogenic autoregulation in normotensive and hypertensive rats," *Can. J. Physiol. Pharmacol.*, vol. 79, pp. 238–245, Mar. 3, 2001.

[31] A. Just and W. J. Arendshorst, "Nitric oxide blunts myogenic autoregulation in rat renal but not skeletal muscle circulation via tubuloglomerular feedback," *J. Physiol.*, vol. 569, pp. 959–974, 2005.

[32] A. P. Somlyo and A. V. Somlyo, "Ca^{2+} sensitivity of smooth muscle and nonmuscle myosin II: Modulated by G proteins, kinases, and myosin phosphatase," *Physiol. Rev.*, vol. 83, pp. 1325–1358, 2003.

[33] V. M. Bolotina, S. Najibi, J. J. Palacino, P. J. Pagano, and R. A. Cohen, "Nitric oxide directly activates calcium-dependent potassium channels in vascular smooth muscle," vol. 368, pp. 850–853, 1994.

[34] K. Tyml, "Role of connexins in microvascular dysfunction during inflammation," *Can. J. Physiol. Pharmacol.*, vol. 89, pp. 1–12, 2011.

Authors', photographs and biographies not available at the time of publication.